GSA DATA REPOSITORY 2020031 https://doi.org/10.1130/G46824.1

Brooke R. Johnson[1], Rosalie Tostevin[1,2], Philip Gopon[1], Jon Wells[1], Stuart A. Robinson[1] and Nicholas J. Tosca[1]

[1]*Department of Earth Sciences, University of Oxford, South Parks Road, Oxford, OX1 3AN, UK*

[2] *Present address: Department of Geological Sciences, University of Cape Town, Rondebosch, Cape Town, 7701, South Africa*

Age Model

The Sherwin Ironstone has been assigned a maximum depositional age of ~1320 Ma on the following basis:

- The Kyalla Mudstone which conformably overlies the Sherwin Ironstone and Moroak Sandstone has a maximum depositional age of 1313 ± 47 Ma based on detrital zircons (Yang et al., 2018).
- The Moroak Sandstone, which is contemporaneous to, and in some locations, conformably underlies the Sherwin Ironstone, has a maximum deposition age between 1345 Ma and 1320 Ma based on detrital zircons (Yang et al., 2018).
- The Velkerri Formation, which conformably underlies the Moroak Sandstone, has a maximum depositional age of between 1349 Ma and 1320 Ma based on detrital zircons (Yang et al. 2018) which overlaps with the whole rock Re-Os age of 1361 ± 21 Ma obtained by Kendall et al., (2009) from the Upper Velkerri Formation.
- All units of the upper Roper Group are intruded by a suite of dolerite dykes and sills which have been assigned a baddeleyite age of 1324 ± 4 Ma using SIMS (Abbott et al., 2001) and 1312.9 ± 0.7 Ma using U–Pb TIMS (Collings et al., 2018).

Ferruginous Sediment Lithofacies

Iron-rich sediments in the upper Roper Group (Sherwin Ironstone and Moroak Sandstone) and the correlative Tijunna Group (Stubb Formation) form a ferruginous zone that crosscuts different lithologies and formations. Here we divide the ferruginous sediments into lithofacies to unravel the processes responsible for their formation.

Clastic lithofacies

The clastic lithofacies has a basin-wide distribution and is found in all studied cores. The clastic facies is typically a ferruginously-cemented medium-grained trough-cross-bedded sub-arenite sandstone. Detrital grains are cemented by pore-filling cements with discrete laminae of waxy olive to leafy-green clays composed of berthierine, Fe-chlorite, Fe-smectite and greenalite and minor serpentines (e.g. antigorite). The depositional setting for the clastic facies is interpreted to be a fluvio-deltaic to marine shore face environment.

Chemical lithofacies

The chemical lithofacies is dominantly formed of laminated green mudstones with minor fine cross bedded sands and siltstones and occurs basin wide. Coated grains occur abundant in localised lenses within the Sherwin Ironstone in the Urapunga, Sherwin Creek and Roper Bar regions. Green clay mineralogy is dominated by authigenic greenalite and berthierine with additional authigenic carbonate-fluorapatite. Depositional environment is interpreted as near shore shoaling bars.

Oxidation and Weathering

Authigenic ferrous silicates of both lithofacies have undergone several stages of oxidation. However, petrographic inspection of oxidised material from core samples reveals that all but the most heavily weathered sediments are still ~90% ferrous-silicates interspersed with individual micron scale goethite and Fe-oxyhydroxide crystals, which cut primary authigenic minerals and fabrics.

In core samples of the Sherwin Ironstone for example, oxidation appears to be related to the presence of porous clastic and kaolinitic layers which may have served as a conduit for oxidising fluids. Oxidation fronts can be clearly seen emanating from fractures and faults whose relationship to the matrix is cross cutting with sharp brittle fractures. In some cases, individual coated grains are bisected by oxidation fronts. This indicates that faulting and fracture occurred after deposition and lithification. Oxidation fronts are also clearly abruptly halted by clay, microbial and organic rich laminae. Often the reaction front is discordant with the primary depositional features and will circle around impermeable areas following fractures or porous laminae.

This initial stage of alteration appears to have then been overprinted by localised re-reduction that followed the same fluid conduits as the initial oxidation. In this stage, both primary Fe-silicates, and secondary oxides are overprinted by Fe-Mg-Mn-carbonates, pyrite, and silica, all of which occur as laminae disruptive grains and nodules, and as diffuse masses that infiltrate previously porous areas of matrix. Petrographic relationships show that this episode of re-reduction clearly post-dates primary deposition and authigensis, and the initial phase of oxidation.

The final stage of alteration is probably related to supergene weathering at or near the surface during the quaternary (Morris 2011, Kastellorizos 2014). This has resulted in the destruction of most primary features via the mobilisation of Fe-oxides and silica from coated grains, and their redistribution throughout the matrix. Rare microscopic remnants of the original Fe-silicate mineralogy can be found as relicts within protected grain nuclei. In the most advanced cases of weathering, heavy silicification has replaced most of the Fe-oxides with quartz and opal. Kastellorizos (2014) and Morris (2011) hypothesise that it was the recent supergene weathering that concentrated iron to economic levels in the ore grade beds.

It is hard to reconcile these alteration features with either deposition of primary authigenic oxides that have then been latterly reduced to ferrous silicates, or mixed ferric/ferrous phase deposition. Considering these observations, the simplest explanation is that the primary authigenic phases were ferrous silicates. All other extensive and pervasive oxidation and alteration took place in later diagenesis and during surface exposure following percolation of alternately oxidising and reducing fluids. These observations are consistent with those made

by Cochrane & Edwards (1960), Morris (2011), Ferenczi et al., (1997) and Kastellorizos (2014).

Extended Methods

Sample Collection

Surface samples were collected from a commercial quarry at Mt McMinn (14°41'57.2"S 134°22'30.6"E, Fig 3, main text) with one sample collected every 1 m across the 8 m thickness of section. Core material was obtained from the Northern Territory Geological Survey core facility in Darwin, and the Geoscience Australia core facility in Canberra. Details of cores sampled, and their geographic locations can be found in Fig 3 of the main text. Samples were collected every ten meters for the full extent of each section with higher resolution scale logging and continuous sampling of important transitions. Cores were graphically logged in decimetre scale and detailed petrographic notes and photographs taken.

Sample Preparation

Samples were cut on a standard industrial rock saw fitted with a diamond blade and water coolant. Samples were ground flat with on a standard industrial grinder fitted with a copper and carborundrum grinding wheel. Samples were then hand lapped with 15 µm Aluminium oxide powder. Samples were attached to pre-lapped glass slides with Struers Epo Fix two part Epoxy resin, or Loctite 365 UV resin. Sections were lapped to a thickness of 30 µm using 15 µm Aluminium Oxide powder, on a Logitech LP50 precision lapping machine. Final polish for SEM work was achieved with 0.3 µm Aluminium Oxide powder, on a Struers Labopol polishing machine. All sample preparation was carried out at the University of Oxford, Department of Earth Sciences, UK.

XRD Peak Correction

All samples were corrected for sample height displacement error, which causes whole-pattern peak shifts, by normalising to the quartz 011 reflection at 3.343 angstroms. In addition to other distinctive diffraction peaks, differentiation of greenalite from berthierine is perhaps clearest in terms of the 002 reflection which, for berthierine occurs at 3.52–3.54 angstroms (Bailey, 1984), and for greenalite occurs at 3.60–3.62 angstroms (Bailey, 1984). With Co radiation, the corresponding diffraction angles of these peaks are suitably separated from one another; all samples contain either one or both of berthierine and greenalite.

References

Abbott ST and Sweet IP, 2001. Measured sections and drillcore logs from the Urapunga and Roper River 1:250 000 mapsheets, Northern Territory. Northern Territory Geological Survey, Technical Report 2001-004.

Bailey, S.W. 1984 in: Brown, G. and Brindley, G.W., Crystal Structures of Clay Minerals and Their X-Ray Identification. 2nd Edition, Mineralogical Society, London, 305-360.

Bhattacharyya, D.P., 1983, Origin of Berthierine in Ironstones: Clays and Clay Minerals, v. 31, p. 173–182,

Cochrane, G.W. Edwards, A.B. 1964. The Roper River oolitic ironstone formations Mineragraph. Invest., Tech. Pap., 1, C.S.I.R.O, Melbourne, p. 28

Collins, A., Farkas, J., Glorie, S., Cox, G., Blades, M.L., Yang, B., Nixon, A., Bullen, M., Foden, J., Dosseto, A., Payne, J.L., Denyszyn, S., Edgoose, C.J., Close, D., Munson, T.J., Menpes, S., Spagnuolo, S., Gusterhuber, J., Sheridan, M., Baruch-Jurado, E. & Close, D., 2018. Orogens to oil: government–industry–academia collaboration to better understand the greater McArthur Basin: in Annual Geoscience Exploration Seminar (AGES) Proceedings, Alice Springs, Northern Territory, 20–21 March 2018. Northern Territory Geological Survey, Darwin. 49–51

Derry, L.A., 2015, Causes and consequences of mid-Proterozoic anoxia: Geophysical Research Letters, v. 42, p. 8538–8546,

Ferenczi PA, 1997. Geological investigation of the Roper River iron deposits. Northern Territory Geological Survey Technical Report GS1997-004.

Harder, H. (1989) Mineral genesis in ironstones: a model based upon laboratory experiments and petrographic observations. In: Phanerozoic Ironstones (Ed. by T. P. Young and W. E. G. Taylor), Spec. Publ. geol. Soc. London, 46, 9-18.

Kastellorizos, P., 2014. Sixth annual report over the roper iron ore and uranium project 2

April 2013 to 1 April 2014, Diamantina Uranium pty ltd.

Kendall B, Creaser RA, Gordon GW and Anbar AD, 2009. Re–Os and Mo isotope systematics of black shales from the Middle Proterozoic Velkerri and Wollogorang Formations, McArthur Basin, northern Australia. Geochimica et Cosmochimica Acta 73, 2534–2558

Lanigan K, Hibbird S, Menpes S and Torkington J, 1994. Petroleum exploration in the Proterozoic Beetaloo Sub-basin, Northern Territory. APEA Journal 34, 674 –691.

Morris, R. C. 2012 Microplaty hematite—its varied nature and genesis, Australian Journal of Earth Sciences, 59:3, 411-434,

Planavsky, N.J., Rouxel, O.J., Bekker, A., Lalonde, S. V., Konhauser, K.O., Reinhard, C.T., and Lyons, T.W., 2010, The evolution of the marine phosphate reservoir: Nature, v. 467, p. 1088–1090

Reinhard, C.T., Planavsky, N.J., Gill, B.C., Ozaki, K., Robbins, L.J., Lyons, T.W., Fischer, W.W., Wang, C., Cole, D.B., and Konhauser, K.O., 2017, Evolution of the global phosphorus cycle: Nature, v. 541, p. 386–389,

Yang, B., Smith, T.M., Collins, A.S., Munson, T.J., Schoemaker, B., Nicholls, D., Cox, G., Farkas, J., and Glorie, S., 2018, Spatial and temporal variation in detrital zircon age provenance of the hydrocarbon-bearing upper Roper Group, Beetaloo Sub-basin, Northern Territory, Australia: Precambrian Research, v. 304, p. 140–155.

Figures and Captions

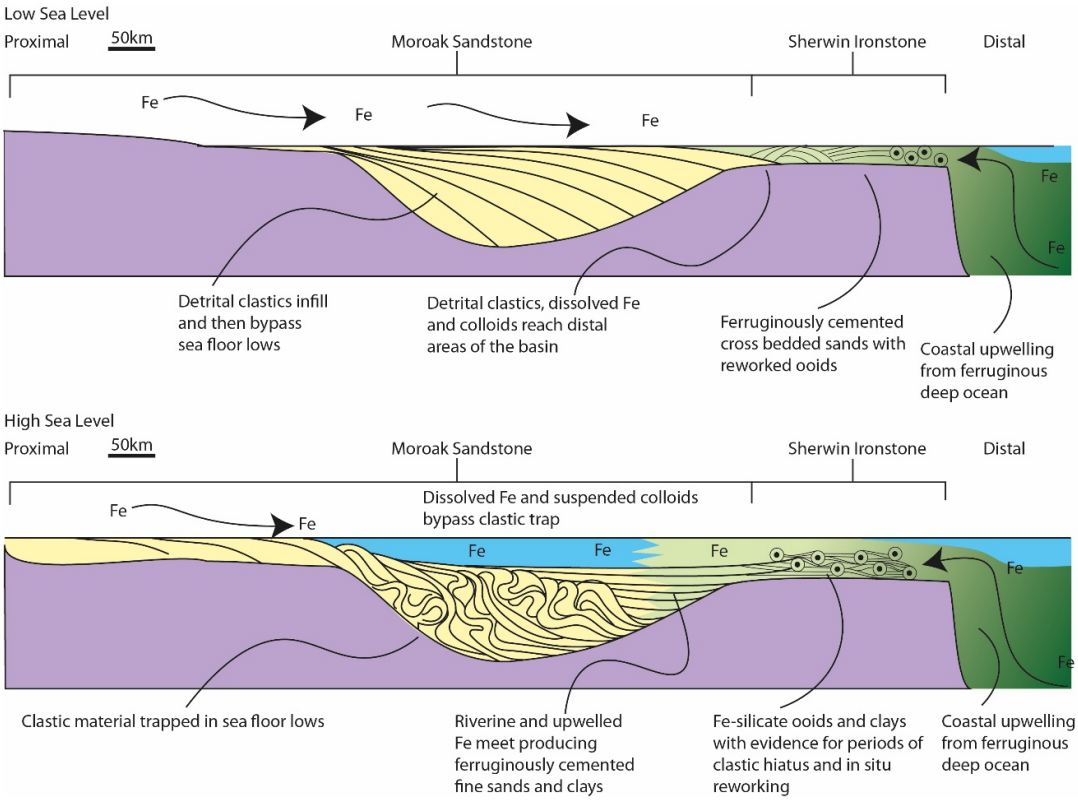

Fig 5. Schematic model showing how clastic trapping can influence the interaction of riverine and upwelling oceanic Fe-bearing water masses to produce the lithologies observed in the Sherwin Ironstone and its stratigraphic equivalents across the Roper Superbasin. *Top*: during relative low sea level, deltaic sands prograde out into the basin. Clastic grains and dissolved and suspended iron bypass the sea floor lows and reach the distal edge of the basin. Here riverine waters interact with upwelling sea water to produce ferruginously cemented sands with ooid and clay-poor beds. *Bottom*: during relatively high sea level, clastic material is captured before it can reach the distal edge of the basin, but suspended and dissolved material bypasses the trap. Upwelling oceanic waters are able to encroach further into the basin and interact with the iron-rich, clastic-poor riverine waters and produce ooids and clay-rich beds in distal areas, and ferruginous-cemented sands in proximal areas.

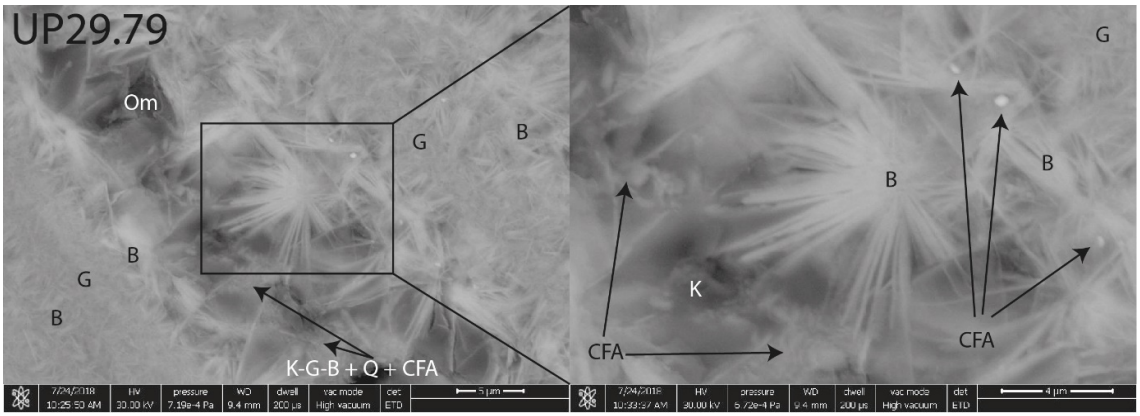

Fig 6. SEM image detailing internal laminae of a pristine ooid. CFA in the organic rich lamina is intergrown with authigenic Fe(II)-silicates. B = berthierine, G = greenalite, K = kaolinite, Q = quartz, OM = organic matter, CFA = calcium-Fluorapatite.

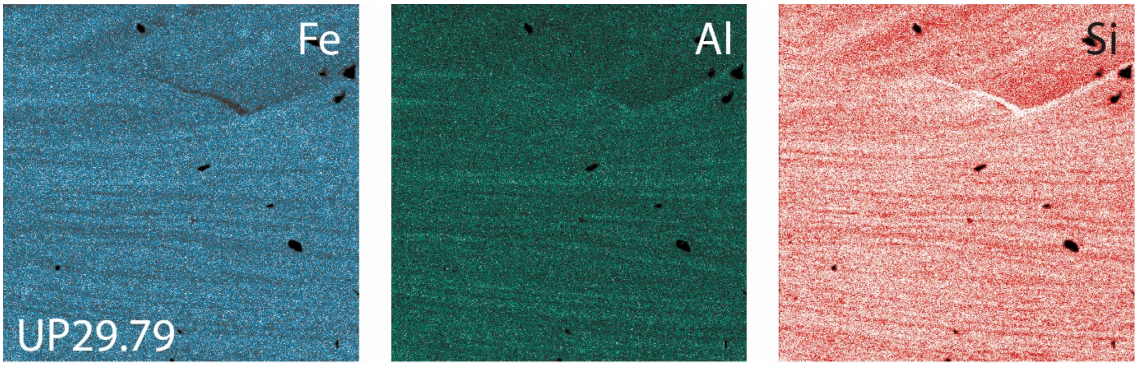

Fig 7. EPMA images of Fe, Al and Si from within a pristine greenalite-berthierine ooid. Greenalite lamina are richer in Fe and Si than berthierine laminae which are rich in Al. Each map is ~200 µm across.

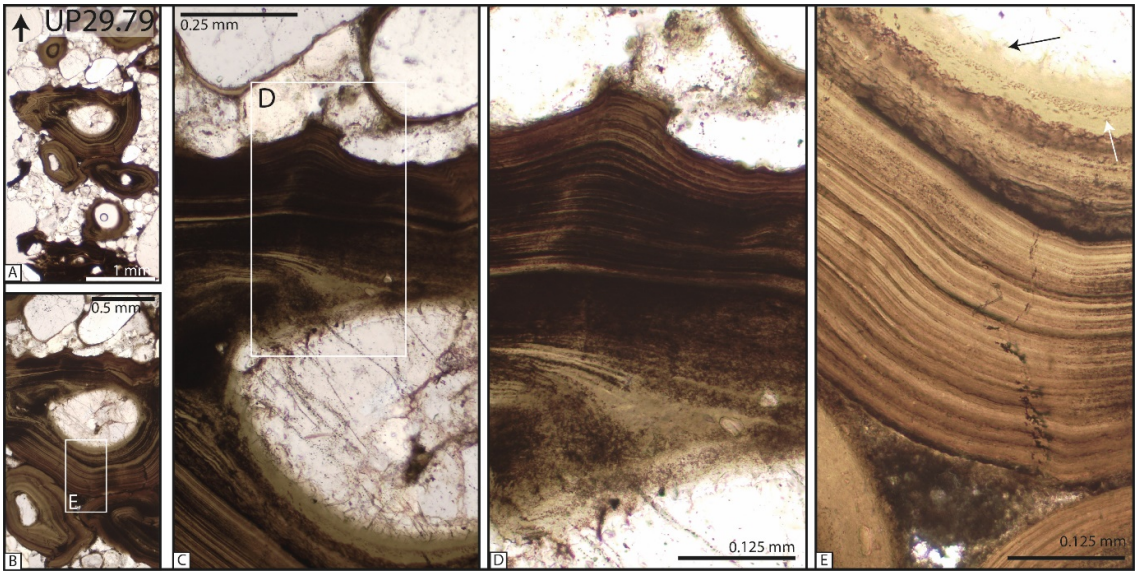

Fig 8. Detail of a greenalite-berthierine ooid in PPL. Matrix is quartz sand with minor feldspar, detrital pyrite and other heavy detritals. Soft spastolithic deformation can be observed clearly throughout e.g., left side of main ooid in A and the lamina in the upper part of D. Greenalite and berthierine can be distinguished in E as light greenalite lamina and darker berthierine lamina. Grains incorporated into laminae are quartz silt and CFA. Black lamina are rich in organic matter which also forms the cross-cutting trail in E. Silica for the Fe-silicate may have also come from quartz nucleus grains as observed in E. Greenalite appears to 'seep' into the outer surface of the quartz grain (black arrow). The original quartz grain surface can be seen as a lamina of kaolinite and haematite (white arrow).